

This manuscript has been authored by UT-Battelle, LLC under Contract No. DE-AC05-00OR22725 with the U.S. Department of Energy. The United States Government retains and the publisher, by accepting the article for publication, acknowledges that the United States Government retains a non-exclusive, paid-up, irrevocable, world-wide license to publish

or reproduce the published form of this manuscript, or allow others to do so, for United States Government purposes. The Department of Energy will provide public access to these results of federally sponsored research in accordance with the DOE Public Access Plan (<http://energy.gov/downloads/oe-public-access-plan>).

## Gaps in Topological Magnon Spectra: Intrinsic vs. Extrinsic Effects

Seung-Hwan Do,<sup>1</sup> Joseph A. M. Paddison,<sup>1</sup> Gabriele Sala,<sup>2</sup> Travis J. Williams,<sup>3</sup> Koji Kaneko,<sup>4,5</sup> Keitaro Kuwahara,<sup>6</sup> A. F. May,<sup>1</sup> Jiaqiang Yan,<sup>1</sup> Michael A. McGuire,<sup>1</sup> Matthew B. Stone,<sup>3</sup> Mark D. Lumsden,<sup>3</sup> and Andrew D. Christianson<sup>1</sup>

<sup>1</sup>*Materials Science and Technology Division, Oak Ridge National Laboratory, Oak Ridge, Tennessee 37831, USA*

<sup>2</sup>*Second Target Station, Oak Ridge National Laboratory, Oak Ridge, Tennessee 37831, USA*

<sup>3</sup>*Neutron Scattering Division, Oak Ridge National Laboratory, Oak Ridge, Tennessee 37831, USA*

<sup>4</sup>*Materials Sciences Research Center, Japan Atomic Energy Agency, Tokai, Ibaraki 319-1195, Japan*

<sup>5</sup>*Advanced Science Research Center, Japan Atomic Energy Agency, Tokai, Ibaraki 319-1195, Japan*

<sup>6</sup>*Institute of Quantum Beam Science, Ibaraki University, Mito, Ibaraki 310-8512, Japan*

For topological magnon spectra, determining and explaining the presence of a gap at a magnon crossing point is a key to characterize the topological properties of the system. An inelastic neutron scattering study of a single crystal is a powerful experimental technique that is widely employed to probe the magnetic excitation spectra of topological materials. Here, we show that when the scattering intensity rapidly disperses in the vicinity of a crossing point, such as a Dirac point, the apparent topological gap size is extremely sensitive to experimental conditions including sample mosaic, resolution, and momentum integration range. We demonstrate these effects using comprehensive neutron-scattering measurements of  $\text{CrCl}_3$ . Our measurements confirm the gapless nature of the Dirac magnon in  $\text{CrCl}_3$ , but also reveal an artificial, i.e. extrinsic, magnon gap unless the momentum integration range is carefully controlled. Our study provides an explanation of the apparent discrepancies between spectroscopic and first-principles estimates of Dirac magnon gap sizes, and provides guidelines for accurate spectroscopic measurement of topological magnon gaps.

Magnons in a honeycomb-lattice ferromagnet have an analogous description to the single-orbital tight-binding model for electrons in graphene. As a result, the magnons in a honeycomb ferromagnet exhibit a linear energy-momentum dispersion near a magnon crossing point, often termed a Dirac magnon [Fig. 1] [1–3]. Observing the Dirac magnon is of intense current interest as a means of assessing potential topological properties. In particular, if spin-orbit coupling (SOC) accompanying a broken inversion symmetry generates a nonzero Dzyaloshinskii–Moriya interaction (DMI), a gap opens at the Dirac crossing point, in close analogy with the spin-orbit-induced semiconducting gap in graphene. This can yield a topologically-protected magnon edge-state with low-dissipation, which results in a non-trivial topological magnon insulator [2–5]. Consequently, experimentally identifying materials with a topological magnon gap (TMG) is a crucial goal, with wide-ranging implications for spin-transport-based technologies such as magnon spintronics [6–8].

Several chromium-based ( $\text{Cr}^{3+}$ ,  $S=3/2$ ) honeycomb ferromagnetic materials have been proposed to host gapped Dirac magnons, namely  $\text{CrBr}_3$ ,  $\text{CrI}_3$ , and  $\text{CrMTe}_3$  ( $M=\text{Si, Ge}$ ) [9–12]. In all of these materials, the key experimental evidence for a TMG has been obtained from single-crystal neutron spectroscopy experiments, which report gaps  $\sim 3$  to 5 meV. However, the origin of the gap opening remains unclear, with proposals including DMI, Kitaev interactions, and magnon-phonon coupling [5, 9, 10, 13–15]. Furthermore, the estimated gaps based upon the DMI and Kitaev interaction

strengths are much bigger than the predicted gap size of first-principle calculations for the small SOC of half-filled  $t_{2g}$  orbitals of  $\text{Cr}^{3+}$  [13, 16]. In this context, accurate neutron spectroscopy experiments can be crucial, because they provide a measurement of the magnon dispersion in 4-dimensional momentum-energy ( $\mathbf{Q}$ - $E$ ) space that can, in principle, be quantitatively compared with calculations. In practice, however, the weakness of the neutron-sample interaction often requires compromises to increase the signal strength, such as the use of many co-aligned single crystals with increased mosaicity, the relaxation of  $\mathbf{Q}$  and  $E$  resolution to gain more neutron flux, and the integration of measured data over a significant range of  $\mathbf{Q}$  and  $E$  to improve counting statistics of the measurement. These approaches to enhance signal can result in spurious findings when the neutron intensity rapidly disperses or has a singularity in  $\mathbf{Q}$ - $E$  space as is the case for a Dirac magnon, and this may in turn cause a significant impact on the observation and estimates of the TMG.

In this letter, we present a detailed analysis of extrinsic effects on spectroscopic estimates of TMG sizes. Our key finding is that a dominant *extrinsic* contribution to the apparent magnon gap occurs if “typical”  $\mathbf{Q}$ -integration ranges are used, which can cause the intrinsic TMG to be substantially overestimated or misdiagnosed. We identify this effect using a simple model. We then present high-resolution neutron spectroscopy measurements on a single crystal of  $\text{CrCl}_3$ . Our results establish  $\text{CrCl}_3$  as an ideal quasi-2D Heisenberg ferromagnet with a gapless Dirac magnon, and provide a compre-

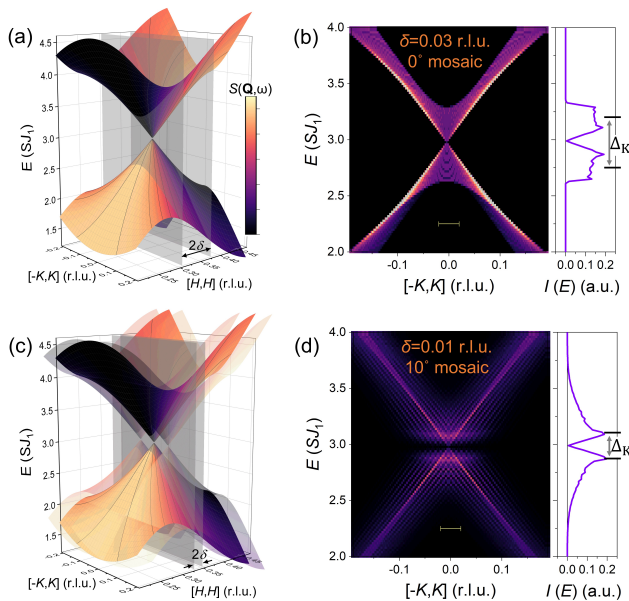


FIG. 1. Demonstration of how data processing parameters ( $Q$ -range of integration) and sample mosaicity lead to the appearance of artificial gaps in a gapless Dirac magnon spectrum. (a) Gapless Dirac magnon dispersion for spins  $S$  on a honeycomb lattice with ferromagnetic nearest-neighbor interaction  $J_1$ . (b) The  $Q$ - $E$  contour map is obtained by integrating over data within the finite orthogonal  $Q$ -range,  $2\delta$  shown in (a). Due to rapid dispersion away from the crossing point, an artificial gap ( $\Delta_K$ ) appears in the spectrum with an apparent size ( $\Delta_K$ , defined as the distance between the two peak centers) that depends on the  $Q$ -integration range. (c) Sample mosaicity generates a broad distribution of off-centered Dirac cones in  $Q$ , and the superposed magnon spectra produces an artificial gap at the K-point. (d) Calculated Dirac magnon spectra for a  $10^\circ$  sample mosaicity with a  $\delta=0.01$  r.l.u.. Data within the yellow bar are integrated to obtain the energy scan at the K-point (far right panels).

hensive map of the excitation spectrum near the Dirac point. However, we also find that an extrinsic magnon gap appears unless the  $Q$ -integration range is carefully controlled. Finally, we reinterpret published spectroscopic studies of  $\text{CrBr}_3$  [11] and  $\text{CrSiTe}_3$  [12], and show that the apparent magnon gaps in these materials likely contain substantial extrinsic contributions. Our results resolve apparent discrepancies between spectroscopic and first-principles estimates of TMG sizes, and provide guidelines for accurate spectroscopic measurement of topological magnon gaps.

Figure 1 shows calculated magnon spectra for a honeycomb-lattice Heisenberg ferromagnet with nearest-neighbor (n.n.) interaction  $J_1$ . This model preserves effective time-reversal magnon symmetry and exhibits a gapless Dirac magnon. As shown in Fig. 1(a), two cone-shaped dispersions touch at a single location in three-dimensional  $Q$ - $E$  space. The linear dispersion near the Dirac point is revealed by taking a slice along the  $[-K, K, 0]$  direction [Fig. 1(b)]. In practice, it is necessary to integrate the intensity over a finite  $Q$ -range (denoted  $2\delta$ ) orthogonal to the slice direction. The gapless Dirac magnon is faithfully reproduced only in the limit  $\delta \rightarrow 0$

[Fig. 1(a)]. In contrast, taking  $\delta = 0.03$  r.l.u. yields an apparent gap of size  $\sim 0.5SJ_1$ , which is 8% of the full bandwidth of  $6SJ_1$  [Fig. 1(b)]. Here, our choice of  $\delta$  is informed by previous experimental studies, in which “typical” values of  $\delta$  are between 0.03 and 0.20 r.l.u. [9–11, 17]. This extrinsic gap occurs because the intensity is averaged over the Dirac cone away from the Dirac point, and is substantial even for small  $\delta$  because the intensity varies rapidly with  $Q$ . This  $Q$ -integration effect is also distinct from the effect of sample mosaicity such as considered for recent study of  $\text{CrI}_3$  [10], which generates a superposition of off-centered Dirac cones [Fig. 1(c)], and causes an additional artificial gap at the Dirac point [Fig. 1(d)].

We investigate extrinsic contributions to the magnon gap using spectroscopic measurements of the van-der-Waals ferromagnet  $\text{CrCl}_3$ , which contains undistorted  $\text{Cr}^{3+}$  honeycomb layers below 150 K (space group  $R\bar{3}$ ) [18, 19].  $\text{CrCl}_3$  has a ferromagnetic spin alignment in the plane in each honeycomb layer below  $T_N = 14$  K [18]. Compared to  $\text{CrBr}_3$  and  $\text{CrI}_3$ , the relatively light Cl ligand atom of  $\text{CrCl}_3$  is likely to give a small SOC and hence anisotropic exchange interactions should also be correspondingly weak and host a gapless Dirac magnon, as suggested by recent neutron-scattering measurements on polycrystalline  $\text{CrCl}_3$  samples [20, 21]. Furthermore, unlike other Cr-halides such as  $\text{CrI}_3$ ,  $\text{CrCl}_3$  can be grown in as a large single crystal with a small sample mosaicity. Consequently,  $\text{CrCl}_3$  is an ideal model system to investigate the impact of extrinsic effects and data treatment on the spin-wave spectrum near the Dirac point.

A  $\text{CrCl}_3$  single crystal with a mosaicity  $< 0.68^\circ$  was grown by re-crystallization of commercial  $\text{CrCl}_3$  powder [22]. The INS data was collected with the SEQUOIA time-of-flight spectrometer [23] at the Spallation Neutron Source located at Oak Ridge National Laboratory. The Fermi choppers were phased for the *high-resolution* mode of SEQUOIA for incident energies  $E_i = 4, 11, \text{ and } 25$  meV [24]. Figure 2(a) shows the measured magnon spectra at 5 K ( $T < T_N$ ). The spectra are composed of one acoustic and one optical magnon branch with an overall magnon bandwidth of 8 meV ( $W_{HK}$ ) in the  $HK$ -plane. The acoustic magnon emanates from the  $\Gamma$  point (0,0,0), and meets the optical magnon at the K-points, exhibiting typical spin-waves for a ferromagnetic honeycomb lattice [2].

To model the observed magnon spectra, we used linear spin-wave theory (LSWT) using the SpinW package [25]. The spin Hamiltonian was modeled with  $\mathcal{H} = J_n \sum_{i,j} S_i S_j - D^z \sum_i (S_i^z)^2$ , for  $S = 3/2$  of  $\text{Cr}^{3+}$ . We consider Heisenberg ( $J_n$ ) exchanges up to the third n.n. interactions in the honeycomb plane and an easy-plane single-ion anisotropy ( $D^z > 0$ ). We exclude bond-dependent exchange interactions (Kitaev and  $\Gamma$  terms) because these would yield different mode energies at different K-points coupled with the aligned spin direction [26], in disagreement with our experimental data. We also note that the symmetry-allowed second n.n. DMI term cannot generate a magnon gap at the K-point for the in-plane magnetic structure with the symmetry operations of exchange matrix for  $R\bar{3}$  structure [17]. The inter-layer cou-

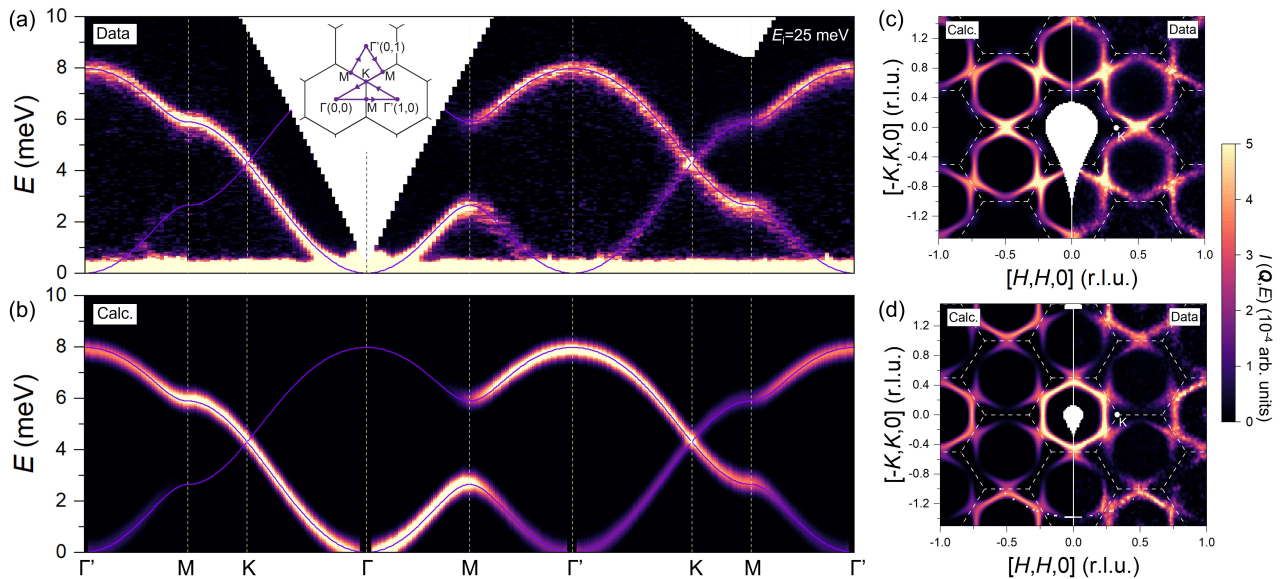


FIG. 2. (a) INS spectra of  $\text{CrCl}_3$  measured at  $T = 5 \text{ K}$  ( $< T_N$ ) along high-symmetry directions as indicated in the  $HK$ -reciprocal space map shown in the inset. Data were obtained by integrating over a thickness of  $Q = 0.024 \text{ \AA}^{-1}$  ( $0.02 \text{ r.l.u.}$  along  $[H, 0, 0]$  in the  $HK$ -plane and  $-2.5 \leq [0, 0, L] \leq 2.5$  along the out-of-plane direction). (b) Corresponding spin-wave calculations convolved with the energy resolution function of the instrument. Constant energy slices for (c)  $E = 6.0 \pm 0.15 \text{ meV}$  and (d)  $E = 2.5 \pm 0.15 \text{ meV}$  are compared with the corresponding calculations.

pling was assumed to be negligible due to the highly two-dimensional spin-wave dispersion (see [24] for a sensitivity of interlayer coupling in spin-wave analysis). The calculated magnon dispersions from the model Hamiltonian were fitted to the experimental dispersion points extracted by fitting a Gaussian function to the INS spectra. The best fit was for  $J_1 = -0.934(5) \text{ meV}$ ,  $J_2 = -0.0302(2) \text{ meV}$ ,  $J_3 = 0.0488(1) \text{ meV}$ , and  $D^z = 0.0100(1) \text{ meV}$  [24]. The dominant n.n. ferromagnetic interaction  $J_1$  is responsible for the formation of the ferromagnetic honeycomb spin-lattice in  $\text{CrCl}_3$ . The single-ion anisotropy was found to be nearly zero, indicating a nearly isotropic  $\text{Cr}^{3+}$  spin. Fig. 2(b-d) show that the calculated spectra reproduce the measured spectra with high fidelity, demonstrating a quasi-two-dimensional Heisenberg ferromagnetic honeycomb spin-lattice for  $\text{CrCl}_3$ . The determined Hamiltonian preserves time-reversal symmetry of magnons, resulting in a gapless Dirac magnon at the K-point.

Details of the magnon spectra near the Dirac point are shown in Fig. 3. In the figure, the magnon spectra are displayed along the radial  $Q$ -direction (parallel to  $[H, H, 0]$ ) with varying transverse  $Q$ -component ( $[-K, K, 0]$ ). The separate acoustic and optical modes intersect at the single  $Q$ -position of the Dirac point  $(\frac{1}{3}, \frac{1}{3}, 0)$ . This sharp band touching is viewed as a nodal point at  $E^{\text{Dirac}} = 4.4 \text{ meV}$  in the horizontal  $Q$ - $E$  slices of the spectra [Fig. 3(b)], representing the shape of a Dirac cone dispersion. Deviating from  $E^{\text{Dirac}}$ , the Dirac point evolves into triangular scattering patterns around K [Fig. 2(c,d)] with modulating intensity across the Dirac point in energy. The variation in intensity is associated with the isospin locked with offset momentum winding around the

Dirac point [26, 27]. As the result, the two conical dispersions having anti-phased winding patterns of intensity meet at the K-point [refer to Fig 1(a)]. When  $Q$  is perpendicular to the radial-direction, the two bands have an identical magnon structure factor, and the Dirac magnon reveals a clear band crossing, as shown in Fig. 3(c), evidencing a gapless Dirac magnon in  $\text{CrCl}_3$ .

As described above, a focal issue in the search for topological properties of the magnon spectrum is identifying the presence of an intrinsic gap (TMG) at the K-point. Here we investigate the impact of  $Q$ -integration range on the spectrum near the Dirac point in  $\text{CrCl}_3$ . Fig. 3(c)-(e) show the results of the differently histogrammed spectra in the vicinity of the K-point while varying the orthogonal momentum-integration range,  $dQ^{\text{rad}}$ . (see Fig. 3(b) for  $dQ^{\text{rad}}$ ). For  $dQ^{\text{rad}} = \pm 0.01$ , the experimental spectrum shows a gapless feature [Fig. 3(c)]. However, a slightly wider integration range with  $dQ^{\text{rad}} = \pm 0.03$  opens an *apparent* gap with  $\Delta_K \sim 0.7 \text{ meV}$  ( $\sim 0.09 W_{HK}$ ) [Fig. 3(d)] and the apparent gap size increases with  $\Delta_K \sim 1.3 \text{ meV}$  ( $0.16 W_{HK}$ ) for  $dQ^{\text{rad}} = \pm 0.06$  [Fig. 3(e)] (see Fig. 3(f) for  $dQ^{\text{rad}}$  dependence of the gap size). The measured spectra are directly compared to the spin-wave calculation from the obtained Hamiltonian parameters, reflecting the resolution function of the SEQUOIA spectrometer for the identical momentum integration ranges. The good agreement between calculations and experiment demonstrates that the apparent gap is fully explained by the choice of  $Q$ -integration range. This artificial gap consistently appears in the radial  $Q$  scan for  $dQ^{\text{trans}}$  range, reflecting the conical shape of dispersion. It is worth noting that this *apparent* gap exhibits a finite

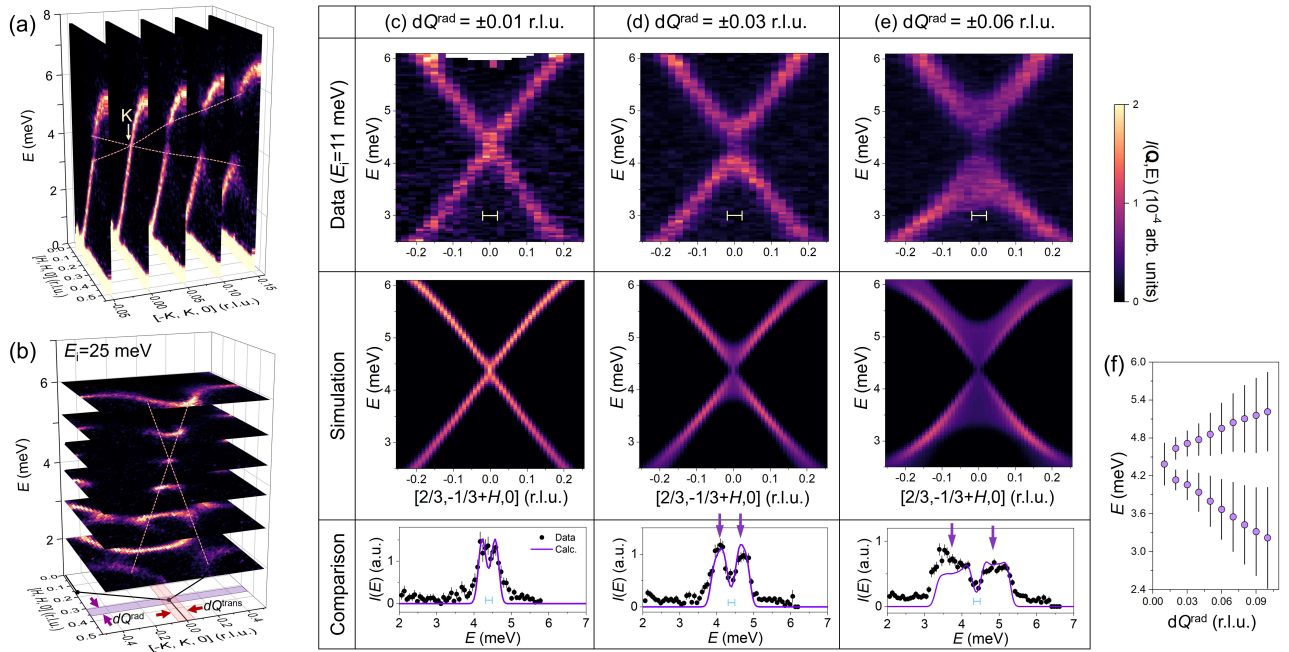


FIG. 3. (a)  $Q$ - $E$  slices along  $[H, H, 0]$ -directions at  $K = -0.05, 0, 0.05, 0.1, \text{ and } 0.15$  for  $[-K, K, 0]$ . Data were obtained by integrating over  $-0.01 \leq K \leq 0.01$  and  $-2.5 \leq L \leq 2.5$ . The dashed lines connect ends of acoustic and optical magnon bands varying with  $[-K, K, 0]$ , which shows a crossing of two magnon bands at a Dirac point,  $K = (\frac{1}{3}, \frac{1}{3}, 0)$ . (b) Constant energy slices of the INS spectra. The dashed lines indicate energy evolution of acoustic and optical magnons along the transverse  $Q$ -direction near the Dirac point. (c-d) Opening an artificial gap at crossing point,  $(\frac{2}{3}, -\frac{1}{3}, 0)$ , with increasing integration range,  $dQ^{\text{rad}}$ . The spectra were collected using high resolution mode for  $E_i = 11$  meV with the SEQUOIA spectrometer, and obtained by integrating over (c)  $dQ^{\text{rad}} = \pm 0.01$  r.l.u., (d)  $dQ^{\text{rad}} = \pm 0.03$  r.l.u., and (e)  $dQ^{\text{rad}} = \pm 0.06$  r.l.u. ( $0.02, 0.06, 0.13 \text{ \AA}^{-1}$ , respectively). The energy-resolution convolved spin-wave spectra are compared in the second and third rows, and are calculated for the identical  $Q$ -integration range as the experimental data. The constant  $Q$ -scans at the Dirac point were compared by integrating over  $dQ^{\text{trans}} = \pm 0.02$  r.l.u. (a yellow bar in the contour map). The blue bar is the instrumental resolution at  $E^{\text{Dirac}} = 4.4$  meV. The peak positions and full-width-at-half maximum are quantified by Gaussian fits and exhibited as points with error-bars, respectively, as a function of  $dQ^{\text{rad}}$  in (f). The distance between the positions indicate the apparent gap size.

spectral intensity within the gap, where the instrumental resolution is smaller than the apparent gap size, which is in contrast to the TMG case showing zero intensity between the peak splitting [24]. Therefore, to clarify TMG, careful comparison of the measured data to the energy-resolution convolved spin-wave calculation including momentum integration range should be performed.

The discussion above has important implications for the ongoing debate regarding the observations of the Dirac magnon gap in other chromium van der Waals honeycomb ferromagnets. The previously used momentum integration range and a large sample mosaic for  $\text{CrBr}_3$  ( $dQ^{\text{trans}} = \pm 0.2$ ) and  $\text{CrI}_3$  (sample mosaic =  $8 \sim 17^\circ$ ), respectively, are likely to cause a large extrinsic gap contribution [9–11], thus the TMGs are possibly overestimated. Figure 4(a) shows the calculated INS spectrum of the spin-wave spectra for  $\text{CrBr}_3$  [11], including the  $Q$ -integration range and instrumental resolution used in Ref. [11]. This calculation assumes *only* Heisenberg interactions ( $J_1 = -1.48$  meV,  $J_2 = -0.08$  meV,  $J_3 = 0.11$ , and  $D^z = -0.02$  meV, from Ref. [11]) with zero DMI. For simplicity, the sample mosaic was assumed to be zero. The resulting spectrum shows the upper and lower magnon spectra having decreased intensities near the Dirac points ( $K_1, K_2$ ), which

reproduces the observed magnon dispersion in Ref. [11]. Noticeably, most of the observed gap, corresponding to the peak splittings  $\sim 4$  meV, in the energy scans at  $K_1$  and  $K_2$  is explained by the orthogonal momentum integration range effect on a pure Heisenberg model, without DMI. As a consequence, the size of the gap at the Dirac point is likely overestimated.

In contrast to time-of-flight spectroscopy measurement on Cr trihalides, topological magnon candidates  $\text{CrMTe}_3$  ( $M=\text{Si, Ge}$ ) were measured using triple-axis spectrometers [12]. For triple-axis measurements, integration ranges are not a concern but resolution effects can be significant, particularly when horizontal focusing is used. Therefore, the observed spectra are strongly coupled with the shape of the resolution function (gray ellipse in Fig. 4(c)). Figure 4(c) exhibits newly calculated spin-wave spectra for  $\text{CrSiTe}_3$  [12], including the resolution calculation for the experiment using Reslib [28]. For the spin-wave calculation, we used *only* Heisenberg spin Hamiltonian parameters ( $J_1 = -1.49$  meV,  $J_2 = -0.15$  meV,  $J_{c1} = -0.07$ ,  $J_{c2} = -0.06$ , and  $D^z = -0.01$  meV, from Ref. [12]) with zero DMI. As can be seen, while the gapless Dirac dispersion parallel to the the ellipse (focused) at  $K_1^{\text{focus}}$  leads to a single peak (gapless), the Dirac dispersions anti-parallel to the ellipse (defocused) at  $K_1^{\text{defocus}}$

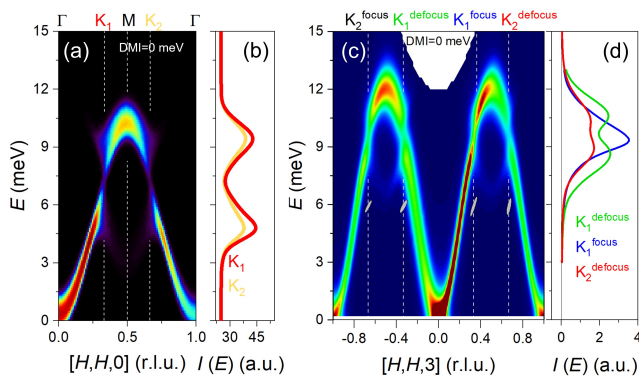


FIG. 4. Calculations of INS spectra for topological magnon candidates, considering extrinsic effects. (a) Calculated spectra for *time-of-flight* spectrometer experiment for CrBr<sub>3</sub> [11]. Spin-waves were calculated for only the Heisenberg Hamiltonian parameters considering the integration range  $dQ^{\text{trans}} = 0.2$  r.l.u. ( $0.23\text{\AA}^{-1}$ ). (b) Calculated energy scans at  $K_1$  and  $K_2$ . (c) Calculated spectra for a *triple-axis* spectrometer experiment for CrSiTe<sub>3</sub> [12]. The spin-wave spectrum was calculated for only the Heisenberg parameters, and convolved with the instrumental energy resolution function for the experimental conditions presented in Ref. [12]. The simulated resolution ellipse functions at the K-points at  $E^{\text{Dirac}} = 10$  meV are indicated with gray ellipse. The K-points are divided into ‘focus’ and ‘defocus’ regions according to the coupling status of the dispersion and resolution ellipse, and the energy scans simulated at  $K_1^{\text{focus}}$ ,  $K_1^{\text{defocus}}$ , and  $K_2^{\text{defocus}}$  are compared in (d).

and  $K_2^{\text{defocus}}$  lead to an apparent gaps in the constant  $Q$ -scans [Fig. 4(d)]. In this case, the defocused resolution condition plays similar role to the orthogonal  $Q$ -integration range in Fig. 3. Confirming the TMG in CrMTe<sub>3</sub> ( $M=\text{Si,Ge}$ ) requires quantitative comparison of the data and the fully resolution-convolved simulation. Assuming that the data in Ref. [12] (Fig.2H) was measured at the focused  $K_1$  ( $\frac{1}{3}, \frac{1}{3}, 3$ ) and defocused  $K_2$  ( $\frac{2}{3}, \frac{2}{3}, 3$ ), our new resolution-convolved spin-wave simulations suggest a DMI  $\sim 0.06$  meV that is a half of the value reported in Ref. [12] (see [24] for details).

In conclusion, revealing and understanding topological magnons are important steps towards the realization of magnon-based electronic devices as well as for the fundamental goal of discovering a topological magnon insulator. To meet these challenges, accurately clarifying and estimating an intrinsic Dirac magnon gap is a critical issue in defining the topological properties, and INS experiments play a key role in this endeavor. In particular, our study provides important guidance for spectroscopic measurements of systems having a singularity or a band crossing where the spectrum rapidly disperses in momentum space. We have shown that instrumental and data-processing effects can introduce an artificial gap, so that accurate estimation of the topological gap size requires careful data histograms and comparison with resolution-convolved calculations. Our results are relevant not only to Dirac magnon gaps, but also to similar Weyl magnon, determining avoided crossing of rattler modes to acoustic phonons [29], and quantifying the life-time of rapidly

decaying phonon spectra [30], where similar effects may be anticipated.

We thank Yixi Su for providing their experimental conditions and Michael E. Manley for useful discussions. This research was supported by the U.S. Department of Energy, Office of Science, Basic Energy Sciences, Materials Science and Engineering Division. Work at the Oak Ridge National Laboratory Spallation Neutron Source was supported by U.S. DOE, Office of Science, BES, Scientific User Facilities Division.

- [1] M. Goerbig and G. Montambaux, “Dirac fermions in condensed matter and beyond,” in *Dirac Matter*, edited by B. Duplantier, V. Rivasseau, and J.-N. Fuchs (Springer International Publishing, Cham, 2017) pp. 25–53.
- [2] S. A. Owerre, *Journal of Physics: Condensed Matter* **28**, 386001 (2016).
- [3] S. S. Pershoguba, S. Banerjee, J. C. Lashley, J. Park, H. Ågren, G. Aepli, and A. V. Balatsky, *Phys. Rev. X* **8**, 011010 (2018).
- [4] R. Chisnell, J. S. Helton, D. E. Freedman, D. K. Singh, R. I. Bewley, D. G. Nocera, and Y. S. Lee, *Phys. Rev. Lett.* **115**, 147201 (2015).
- [5] E. Aguilera, R. Jaeschke-Ubierno, N. Vidal-Silva, L. E. F. F. Torres, and A. S. Nunez, *Phys. Rev. B* **102**, 024409 (2020).
- [6] Z.-X. Li, Y. Cao, and P. Yan, *Physics Reports* **915**, 1 (2021), topological insulators and semimetals in classical magnetic systems.
- [7] D. Malz, J. Knolle, and A. Nunnenkamp, *Nature communications* **10**, 1 (2019).
- [8] A. Rückriegel, A. Brataas, and R. A. Duine, *Phys. Rev. B* **97**, 081106 (2018).
- [9] L. Chen, J.-H. Chung, B. Gao, T. Chen, M. B. Stone, A. I. Kolesnikov, Q. Huang, and P. Dai, *Phys. Rev. X* **8**, 041028 (2018).
- [10] L. Chen, J.-H. Chung, M. B. Stone, A. I. Kolesnikov, B. Winn, V. O. Garlea, D. L. Abernathy, B. Gao, M. Augustin, E. J. G. Santos, and P. Dai, *Phys. Rev. X* **11**, 031047 (2021).
- [11] Z. Cai, S. Bao, Z.-L. Gu, Y.-P. Gao, Z. Ma, Y. Shangguan, W. Si, Z.-Y. Dong, W. Wang, Y. Wu, D. Lin, J. Wang, K. Ran, S. Li, D. Adroja, X. Xi, S.-L. Yu, X. Wu, J.-X. Li, and J. Wen, *Phys. Rev. B* **104**, L020402 (2021).
- [12] F. Zhu, L. Zhang, X. Wang, F. J. dos Santos, J. Song, T. Mueller, K. Schmalzl, W. F. Schmidt, A. Ivanov, J. T. Park, J. Xu, J. Ma, S. Lounis, S. Blügel, Y. Mokrousov, Y. Su, and T. Brückel, *Science Advances* **7**, eabi7532 (2021).
- [13] Y. O. Kvashnin, A. Bergman, A. I. Lichtenstein, and M. I. Katsnelson, *Phys. Rev. B* **102**, 115162 (2020).
- [14] P. Delugas, O. Baseggio, I. Timrov, S. Baroni, and T. Gorni, *arXiv preprint arXiv:2105.04531* (2021).
- [15] I. Lee, F. G. Utermohlen, D. Weber, K. Hwang, C. Zhang, J. van Tol, J. E. Goldberger, N. Trivedi, and P. C. Hammel, *Phys. Rev. Lett.* **124**, 017201 (2020).
- [16] P. P. Stavropoulos, X. Liu, and H.-Y. Kee, *Phys. Rev. Research* **3**, 013216 (2021).
- [17] B. Yuan, I. Khait, G.-J. Shu, F. C. Chou, M. B. Stone, J. P. Clancy, A. Paramekanti, and Y.-J. Kim, *Phys. Rev. X* **10**, 011062 (2020).
- [18] M. A. McGuire, G. Clark, S. KC, W. M. Chance, G. E. Jellison, V. R. Cooper, X. Xu, and B. C. Sales, *Phys. Rev. Materials* **1**, 014001 (2017).

- [19] A. Glamazda, P. Lemmens, S.-H. Do, Y. S. Kwon, and K.-Y. Choi, *Phys. Rev. B* **95**, 174429 (2017).
- [20] L. Chen, M. B. Stone, A. I. Kolesnikov, B. Winn, W. Shon, P. Dai, and J.-H. Chung, *2D Materials* **9**, 015006 (2021).
- [21] J. A. Schneeloch, Y. Tao, Y. Cheng, L. Daemen, G. Xu, Q. Zhang, and D. Louca, arXiv preprint arXiv:2110.10771 (2021).
- [22] A. F. May, J. Yan, and M. A. McGuire, *Journal of Applied Physics* **128**, 051101 (2020).
- [23] G. E. Granroth, A. I. Kolesnikov, T. E. Sherline, J. P. Clancy, K. A. Ross, J. P. C. Ruff, B. D. Gaulin, and S. E. Nagler, *Journal of Physics: Conference Series* **251**, 012058 (2010).
- [24] “See supplemental material for additional data and analysis.”.
- [25] S. Toth and B. Lake, *Journal of Physics: Condensed Matter* **27**, 166002 (2015).
- [26] M. Elliot, P. A. McClarty, D. Prabhakaran, R. Johnson, H. Walker, P. Manuel, and R. Coldea, *Nature Communications* **12**, 3936 (2021).
- [27] S. Shivam, R. Coldea, R. Moessner, and P. McClarty, arXiv preprint arXiv:1712.08535 (2017).
- [28] E. Farhi, Y. Debab, and P. Willendrup, *Journal of Neutron Research* **17**, 5 (2014).
- [29] M. Christensen, A. B. Abrahamsen, N. B. Christensen, F. Juranyi, N. H. Andersen, K. Lefmann, J. Andreasson, C. R. Bahl, and B. B. Iversen, *Nature materials* **7**, 811 (2008).
- [30] E. Xiao, H. Ma, M. S. Bryan, L. Fu, J. M. Mann, B. Winn, D. L. Abernathy, R. P. Hermann, A. R. Khanolkar, C. A. Dennett, *et al.*, arXiv preprint arXiv:2202.11041 (2022).

# Supplemental material for “Gaps in Topological Magnon Spectra: Intrinsic vs. Extrinsic Effects”

Seung-Hwan Do,<sup>1</sup> Joe A. Paddison,<sup>1</sup> Gabriele Sala,<sup>2</sup> Travis J. Williams,<sup>3</sup> Koji Kaneko,<sup>4,5</sup> Keitaro Kuwahara,<sup>6</sup> A. F. May,<sup>1</sup> Jiaqiang Yan,<sup>1</sup> Michael A. McGuire,<sup>1</sup> Matthew B. Stone,<sup>3</sup> Mark D. Lumsden,<sup>3</sup> and Andrew D. Christianson<sup>1</sup>

<sup>1</sup>Materials Science and Technology Division, Oak Ridge National Laboratory, Oak Ridge, Tennessee 37831, USA

<sup>2</sup>Second Target Station, Oak Ridge National Laboratory, Oak Ridge, Tennessee 37831, USA

<sup>3</sup>Neutron Scattering Division, Oak Ridge National Laboratory, Oak Ridge, Tennessee 37831, USA

<sup>4</sup>Materials Sciences Research Center, Japan Atomic Energy Agency, Tokai, Ibaraki 319-1195, Japan

<sup>5</sup>Advanced Science Research Center, Japan Atomic Energy Agency, Tokai, Ibaraki 319-1195, Japan

<sup>6</sup>Institute of Quantum Beam Science, Ibaraki University, Mito, Ibaraki 310-8512, Japan

## I. EXPERIMENTAL DETAILS AND SPECTRAL SIMULATION METHODS

A single piece of CrCl<sub>3</sub> single crystal (mass: 0.88g and dimension: 12 × 12 × 4 mm<sup>2</sup>) was aligned with  $[H, K, 0]$  in the horizontal scattering plane for the inelastic neutron scattering (INS) measurements (see Fig. S1(a)). The sample was sealed within an aluminum can under an atmosphere of helium exchange gas at room temperature. Figure S1(b) and (c) show the elastic scattering for the  $(H, K, 1)$  and  $(H, 0, L)$  planes. Sharp magnetic reflections appear as magnetic satellite peaks with the ordering wave vector  $\mathbf{Q}_m = (0, 0, \frac{3}{2})$  in the  $R\bar{3}$  rhombohedral crystal structure, representing the alternative magnetic stacking order of the ferromagnetic honeycomb lattice. The rocking scan for  $\mathbf{Q} = (3, 0, 0)$  Bragg reflection was fitted with a Gaussian function, as shown in Fig. S1(d), which gives the full-width at half-maximum (FWHM)  $\sim 0.68^\circ$ , indicating the sample mosaicity is smaller than  $\sim 0.68^\circ$ .

The INS data were obtained at  $T = 5$  K using the SEQUOIA time-of-flight spectrometer located at the Oak Ridge National Laboratory (ORNL). The Fermi chopper was set to 120 Hz, 180 Hz, and 240 Hz for  $E_i = 4, 11,$  and 25 meV, which give FWHM = 0.11, 0.24, and 0.65 meV of resolution at the elastic line ( $E=0$  meV), respectively. For  $E_i = 25$  meV, measurements were performed by rotating the sample through 180° about its vertical axis with 0.5° steps. For  $E_i = 11$  meV, measurements were performed by rotating the sample 2 × 50° with 1° step covering two K-points at  $(-1, 2, 0)$  and  $(2, -1, 0)$  (see Fig. S2(a)). The  $E_i = 4$  meV data was measured by rotating the sample through 35° about its vertical axis to cover  $\mathbf{Q}$  along the  $[H, 0, 0]$ -direction. Data were reduced and analyzed using the Mantid [1], Dave [2], and Horace [3] software packages.

Spin-wave spectra were calculated using the SpinW package [4]. In comparison to measured spectra, the orthogonal integration range  $d\mathbf{Q}$  was accounted for by averaging over the resolution convoluted  $\mathbf{Q}$ - $E$  spectra at  $\sim 10$   $\mathbf{Q}$ -points per  $0.01\text{\AA}^{-1}$  within the range. The triple-axis spectroscopy simulations shown in Fig.4(c)(d) of the main text were performed using ResLib [5] with the resolution function calculation using the Popovici method [6] using the experimental parameters of the IN8 spectrometer used in Ref.[7].

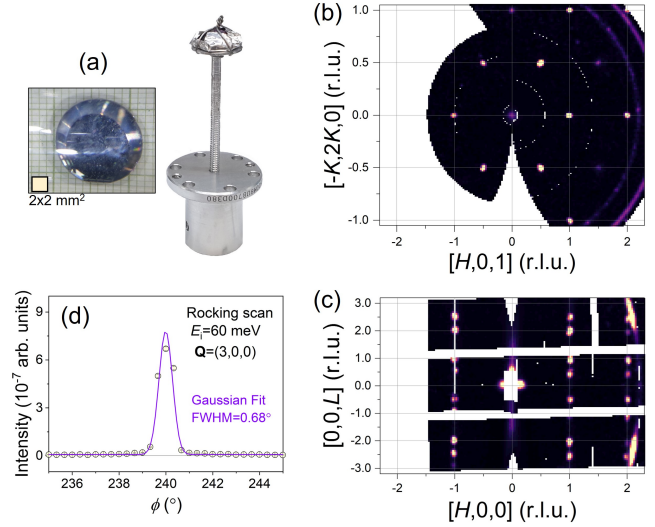


FIG. S1. (a) A picture of aligned CrCl<sub>3</sub> single crystal used for INS measurements. Elastic scattering for (b)  $[H, K, 1]$  and (c)  $[H, 0, L]$  were obtained from SEQUOIA using  $E_i = 25$  meV. Nuclear reflections appear at  $-H + K + L = 3m$  ( $m = \text{integer}$ ) with reverse-obverse twins for  $R\bar{3}$  structure. Magnetic reflections appear with a propagation vector  $\mathbf{Q}_m = (0, 0, \frac{3}{2})$ . The ring-patterns are scattering from the aluminum sample holder. (d) A rocking scan for the Bragg reflection at  $\mathbf{Q} = (3, 0, 0)$  using  $E_i = 60$  meV. The solid line is the Gaussian fit to the data.

## II. DATA SYMMETRIZATION AND CONFIRMATION OF GAPLESS DIRAC MAGNON

While unsymmetrized data was used for  $E_i = 25$  meV to analyze the linear spin-wave theory and to make figures shown in the main text,  $E_i = 11$  meV and 4 meV data were symmetrized using symmetry operations of the Laue class of the  $R\bar{3}$  to enhance statistics. Figure S2 shows a comparison between unsymmetrized and symmetrized data for  $E_i = 11$  meV. The shown magnon spectra in the symmetrized data exhibits the same  $\mathbf{Q}$ - $E$  pattern as the unsymmetrized data, but the signal to noise ratio is improved.

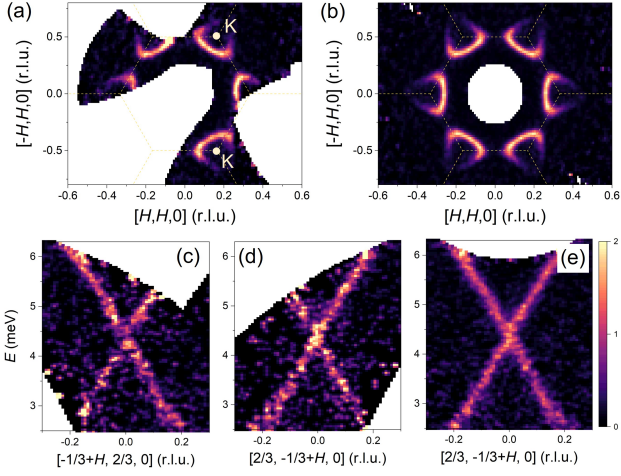


FIG. S2. Comparison of INS data for  $E_i=11$  meV with and without symmetrization. (a) The unsymmetrized constant energy slice data for  $E = [2.85, 3.15]$  meV and (b) corresponding symmetrized data. Unsymmetrized transverse  $Q$ -scans for the two K-points at (c)  $Q = (-\frac{1}{3}, \frac{2}{3}, 0)$  and (d)  $Q = (\frac{2}{3}, -\frac{1}{3}, 0)$  and (e) corresponding symmetrized data at  $(\frac{2}{3}, -\frac{1}{3}, 0)$  were obtained by integrating over  $dQ^{\text{rad}} = \pm 0.01$  and  $-2.5 \leq L \leq 2.5$ .

### III. SPIN-WAVE FITTING RESULTS AND DETERMINATION OF THE HAMILTONIAN PARAMETERS

Experimental dispersions were extracted by fitting Gaussian functions to the constant momentum scans for  $E_i = 25$  meV and 11 meV data along the high symmetry directions (see Fig. S3(b)). 570 dispersion points were obtained from the both  $E_i = 11$  and 25 meV energy spectra (filled circles in Fig. S3(c)), and used for fitting the spin-wave dispersions for the spin Hamiltonian model [Fig. S3(c)],

$$\begin{aligned} \mathcal{H}_0 = & J_1 \sum_{ij} S_i S_j + J_2 \sum_{ij} S_i S_j + J_3 \sum_{ij} S_i S_j \\ & + J_{\text{int}} \sum_{ij} S_i S_j - D^z \sum_i (S_i^z)^2. \end{aligned} \quad (1)$$

This Hamiltonian model describes Heisenberg exchanges up to third nearest neighbor (n.n.) interactions ( $J_n$ ) in a honeycomb layer, Heisenberg n.n. inter-layer interaction ( $J_{\text{int}}$ ) along  $c$ -axis, and easy-plane single-ion anisotropy ( $D^z > 0$ ) (see Fig. S3(a) for the exchange paths). Due to the highly two-dimensional magnon spectra, out-of-plane spin interactions were assumed to be negligible and for simplicity  $J_{\text{int}} = 0.001$  meV was used to stabilize the antiferromagnetic layer order (see below for sensitivity of the  $\chi^2$  on  $J_{\text{int}}$ ).

For fitting the spin-wave dispersion, the  $\chi^2$  optimization function was defined as following,

$$\chi^2 = \frac{1}{n} \sum_i \frac{(E_i^{\text{obs}} - E_i^{\text{calc}})^2}{\sigma_i^2}, \quad (2)$$

where  $E_i^{\text{obs}}$  and  $E_i^{\text{calc}}$  indicate observed and calculated dispersion energies, and  $n$  and  $\sigma_i$  indicate the number of dis-

persion points and standard deviation in the observed dispersion. The fitting of the Hamiltonian parameters to minimize the  $\chi^2$  was performed using the algorithm implemented in the SpinW package [4]. The comparison of the calculated dispersion for the optimized parameters to experimental dispersion is shown in Fig. S3(c), and shows a good agreement. In addition, Fig. S3(d) shows a comparison of the extracted magnon scattering intensity with the spin-wave calculation: the good agreement indicates the existence of isotropically or randomly

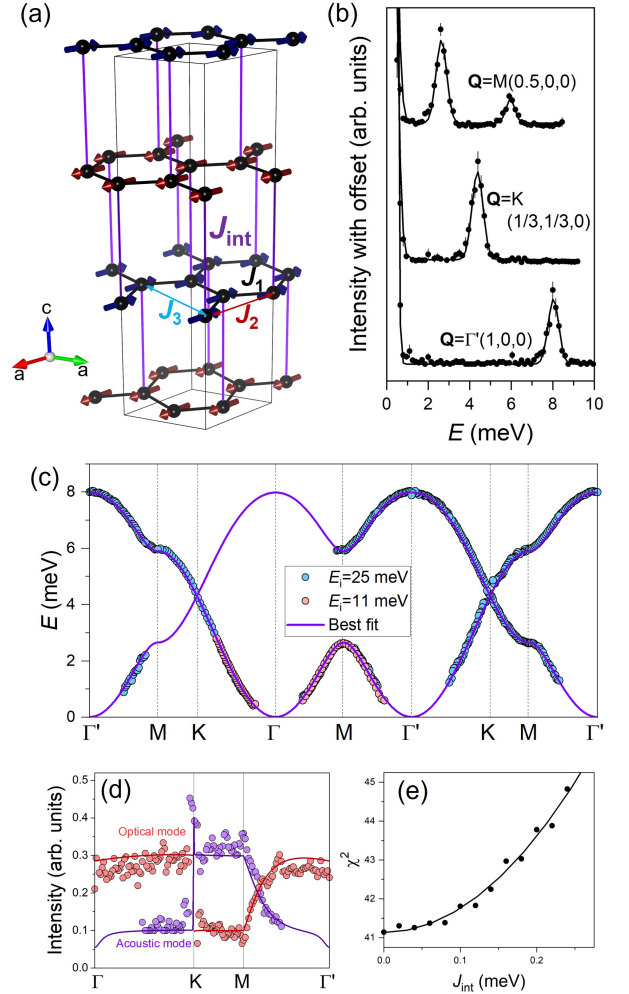


FIG. S3. (a) Magnetic structure and exchange paths for  $\text{CrCl}_3$ . Ferromagnetic moments are aligned in the  $ab$ -plane and antiferromagnetically stacked along the  $c$ -axis. The exchange paths are labeled. (b) Constant momentum scans at the high symmetry points in the Brillouin zone (dots). The black solid lines indicate the Gaussian fitting results on the elastic ( $E = 0$ ) and inelastic ( $E \neq 0$ ) excitation peaks. (c) Comparison between experimental dispersion points from  $E_i = 25$  meV (blue filled circles) 11 meV (pink filled circles) and calculated dispersion (solid purple line) from the best fitting result. (d) Extracted intensity of acoustic (violet dot) and optical (red dot) modes and comparison to LSWT calculation (solid lines). The black arrow indicates the intensity at the K-point. (e) The  $\chi^2$  value as a function of the  $J_{\text{int}}$  interaction strength. The black solid line indicates the parabolic fitting result.



distributed magnetic domains in the plane without preferred orientation.

To check the sensitivity of the inter-layer interaction to the obtained parameters, Fig. S3(e) shows the  $\chi^2$  values of the dispersion points as a function of the  $J_{\text{int}}$  interaction strength with fixed other parameters. The antiferromagnetic interaction was only considered to stabilize the alternative stacking order ground state. The minimum  $\chi^2$  appears near  $J_{\text{int}} \sim 0$  meV, and the  $\chi^2$  shows parabolic increase with increasing  $J_{\text{int}}$ . The graphical errorbar estimation on the local  $\chi^2$  minimum gives the error of  $J_{\text{int}}$  with  $\sim 0.13$  meV [8], corresponding to the sensitivity of the parameter on the spin-wave fitting result. Due to the small number of interaction paths for  $J_{\text{int}}$  (number of interactions on a single spin:  $\#J_{\text{int}} = 1$ ) [Fig. S3], the spin-wave can be less-sensitive to varying the  $J_{\text{int}}$ , compared to other exchanges paths for fixed values of exchange ( $\#J_1 = 3$ ,  $\#J_2 = 6$ , and  $\#J_3 = 3$ ).

#### IV. LOW ENERGY MAGNON SPECTRA: GAPLESS DISPERSION AT $\Gamma$ -POINT AND DISPERSION-LESS SPIN-WAVE ALONG $L$

The low-energy spectra near the zone center (ZC) shown in Fig. S4(a) reveals a quadratic dispersion as expected for a ferromagnetic spin-wave,  $E \propto A\mathbf{Q}^2 + \Delta_{\Gamma}$ , where  $A$  and  $\Delta_{\Gamma}$  are the spin-wave stiffness and magnon gap at the ZC. The low-energy magnon dispersion for energy transfers less than 1.2 meV, measured in the  $E_i=4$  meV configuration, were fitted with the function, which yields  $A=17.14(49)$  and  $\Delta_{\Gamma}=0.00(1)$  meV. The resulting gapless (Goldstone) mode ( $\Delta_{\Gamma} \sim 0$  meV) indicates the preserved U(1) symmetry of Cr spins. This gapless feature is in contrast to the other chromate trihalide materials [9, 10], which emphasizes the importance of the ligand atom's SOC in determining the magnetic anisotropy of the systems [11]. Figure S4(b) shows no discernible dispersion along  $[0.12, 0, L]$  near the ZC. Also, no dispersion along  $[0, 0, L]$  through the ZC is detected within instrumental resolution (FWHM = 0.24 meV at  $E = 0$  meV for  $E_i = 11$  meV) [Fig S4(c)]. The bandwidth along the  $L$ -direction is smaller than the instrumental resolution  $W_L < \text{FWHM}/2 \sim 0.12$  meV, corresponding to less than 1.5% of  $W_{HK}$ , indicating highly two-dimensional spin interactions in  $\text{CrCl}_3$ .

#### V. DIRAC MAGNON ALONG THE RADIAL DIRECTION

In this section, we investigate the Dirac magnon spectra along a radial direction through the K-point with different orthogonal  $\mathbf{Q}$ -integration ranges  $d\mathbf{Q}^{\text{trans}} = \pm 0.05$  r.l.u. and  $\pm 0.2$  r.l.u. (see Fig.2(b) in the main text for definition of  $d\mathbf{Q}^{\text{trans}}$ ). These  $d\mathbf{Q}^{\text{trans}}$  values are typical  $\mathbf{Q}$ -integration ranges that were used for Ref. [7, 12]. Figure S5 shows the magnon spectra along the  $[2H, -H, 0]$ -direction (equivalent direction to the  $[H, H, 0]$ -direction) for the different  $d\mathbf{Q}^{\text{trans}}$  sizes. As the  $d\mathbf{Q}^{\text{trans}}$  increases, the magnon dispersion appears to open a gap at the K-point,  $(\frac{2}{3}, -\frac{1}{3}, 0)$ : while the constant momentum scan for  $d\mathbf{Q}^{\text{trans}}=0.01$ , the data for  $d\mathbf{Q}^{\text{trans}} = \pm 0.05$  shows two

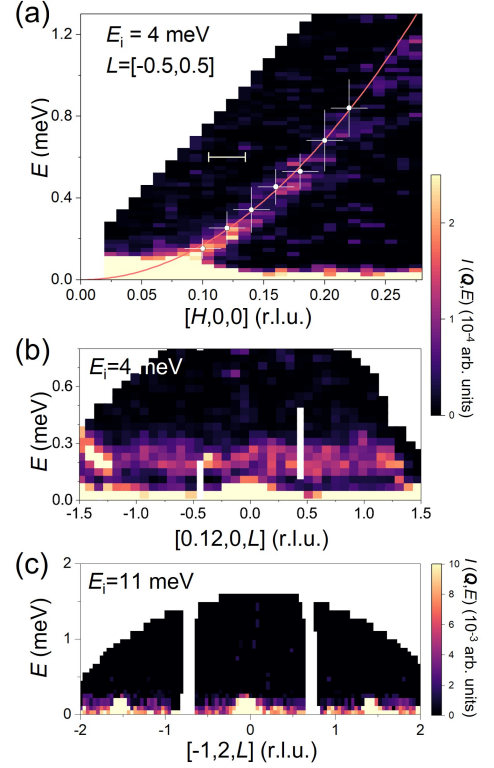


FIG. S4. (a) Low-energy spectrum near the magnetic zone center at  $\Gamma$  (0,0,0) along  $[H, 0, 0]$ . The low-energy dispersion points and its energy line-widths were extracted by Gaussian fits to the constant momentum scans and are exhibited as points with vertical error-bars. The horizontal error-bars indicate integration range for the constant momentum scans. Solid line indicates a gapless biquadratic ferromagnetic spin-wave dispersion,  $E \propto A\mathbf{Q}^2 + \Delta_{\Gamma}$ . (b) Magnon spectra along  $[0.12, 0, L]$  with integration range marked by the bar in (a). (c) Low-energy spectrum near the magnetic zone centers at  $\mathbf{Q} = (-1, 2, -\frac{3}{2})$ ,  $(-1, 2, 0)$ , and  $(-1, 2, \frac{3}{2})$  along  $[0, 0, L]$ .

separated peaks with gap  $\Delta_K \sim 0.5$  meV. The measured spectra were compared to the spin-wave calculations for the determined Hamiltonian parameters in the Fig. S5(d)(e), and the observed gapless and gaped spectra for  $d\mathbf{Q}^{\text{trans}} = \pm 0.01$  and  $\pm 0.05$  are closely reproduced by the pure Heisenberg model ( $J_1 - J_2 - J_3$  model). These results confirm that the orthogonal integration range for the radial  $\mathbf{Q}$ -direction produces an extrinsic gap, same as the transverse direction discussed in the main text.

On the other hand, the momentum integration range  $d\mathbf{Q}^{\text{trans}} = \pm 0.2$  covers nearly half of the Brillouin zone, and the obtained spectra may not reflect the localized spectrum near the K-point. Thus, the shown spectra in Fig. S5(c) and (f) show a very broadened excitation due to the widely averaged spectral weight of the acoustic and optical modes. Accordingly, the constant momentum scan shows two broad peaks with a separation of  $\sim 3$  meV for the gapless spin-wave model, which represents spectral centers of the averaged acoustic and optical modes' spectral weights, not corresponding to the Dirac magnon gap. Therefore, such a large momentum in-

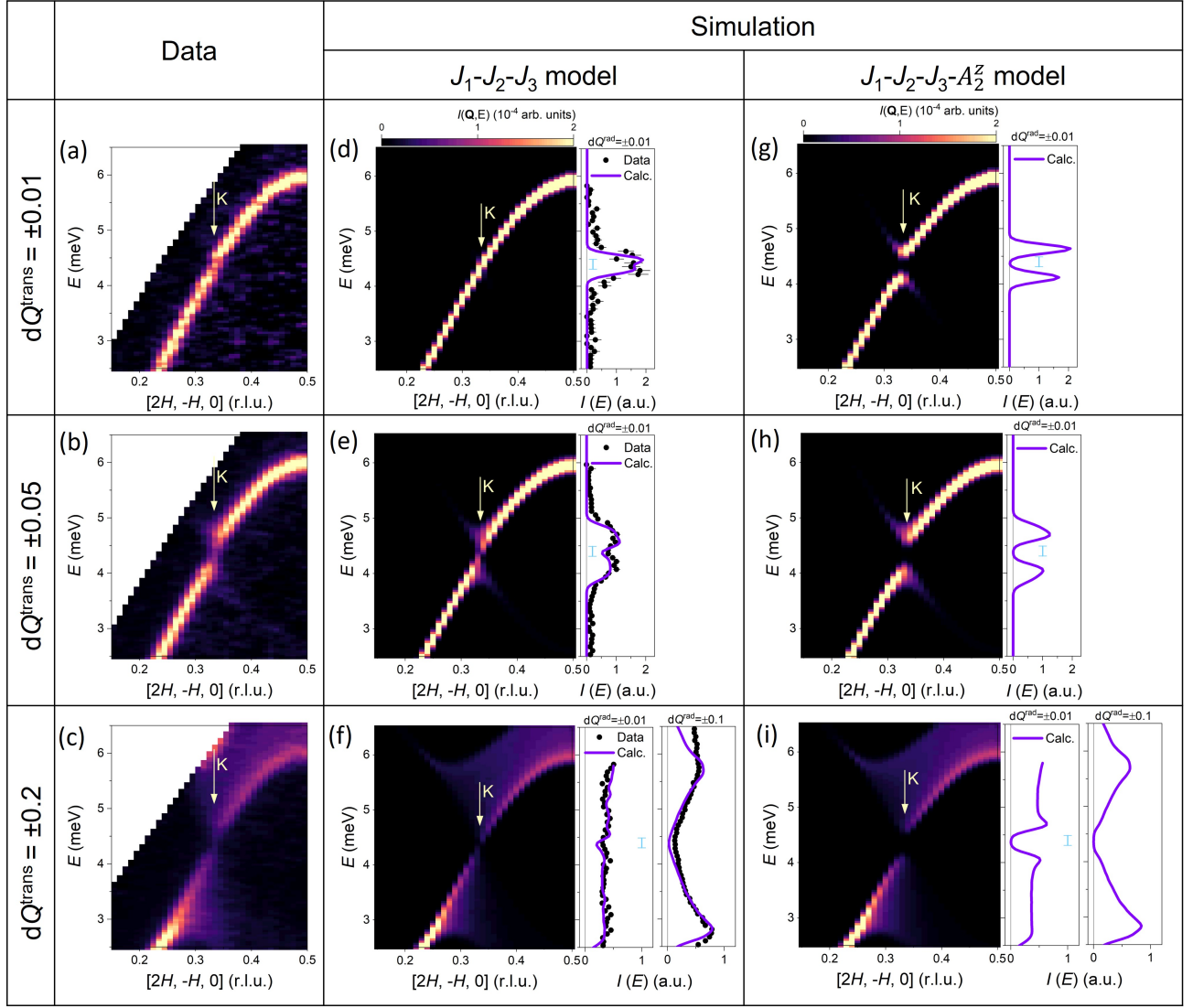


FIG. S5. Dependence of the apparent scattering at the Dirac point along radial  $Q$ -direction on the range of momentum integration. (a-c) The INS spectra were measured using high resolution mode with  $E_i = 11$  meV with the SEQUOIA spectrometer, with varying the orthogonal momentum integration range  $dQ^{\text{trans}} = \pm 0.01, 0.05,$  and  $0.2$  r.l.u. ( $0.012, 0.061$   $0.244\text{\AA}^{-1}$ , respectively) and  $-2.5 \leq L \leq 2.5$  r.l.u.. The spin-wave spectra were calculated for the determined Hamiltonian of the  $J_1 - J_2 - J_3$  model (d-f) and the  $J_1 - J_2 - J_3 - A_2^z$  model (g-i) with the identical  $Q$ -integration ranges. Blue bars in the figure indicate the instrumental resolution at  $E^{\text{Dirac}}$ .

tegration range should not be used to investigate the Dirac magnon spectra.

To compare the observed apparent gap with an intrinsic magnon gap arising from the well-known topological magnon example, we assumed a ferromagnetic spin structure aligned along the  $c$ -axis, same as in the  $\text{CrBr}_3$ ,  $\text{CrI}_3$ , and  $\text{CrMTe}_3$  ( $M=\text{Si,Ge}$ ), and introduced the second n.n. DMI ( $A_2^z$ ) along the  $z$ -axis to the original spin Hamiltonian model ( $\mathcal{H}_0$ ). Then, the new Hamiltonian ( $\mathcal{H}_1$ ) is

$$\mathcal{H}_1 = \mathcal{H}_0 + \sum_{ij} A_2^z \cdot (S_i \times S_j). \quad (3)$$

Here we considered  $A_2^z = J_2 = 0.03$  meV, corresponding to  $\sim 3\%$  of  $J_1$ , and the resulting spin-wave calculations are exhibited in Fig. S5(g-i). The DMI breaks time-reversal

symmetry of magnon, which results in a clear peak splitting from an *intrinsic* gap for all the orthogonal  $Q$  integration values [13]. Noticeably, this intrinsic magnon gap features almost zero scattering intensity at the  $E^{\text{Dirac}}$  regardless of the size of the momentum integration range, in contrast to the pure Heisenberg  $J_1 - J_2 - J_3$  model. This further indicates how the intrinsic gap and the spurious gap can appear differently in the measured spectra where energy resolution is sufficiently smaller than the intrinsic magnon gap.

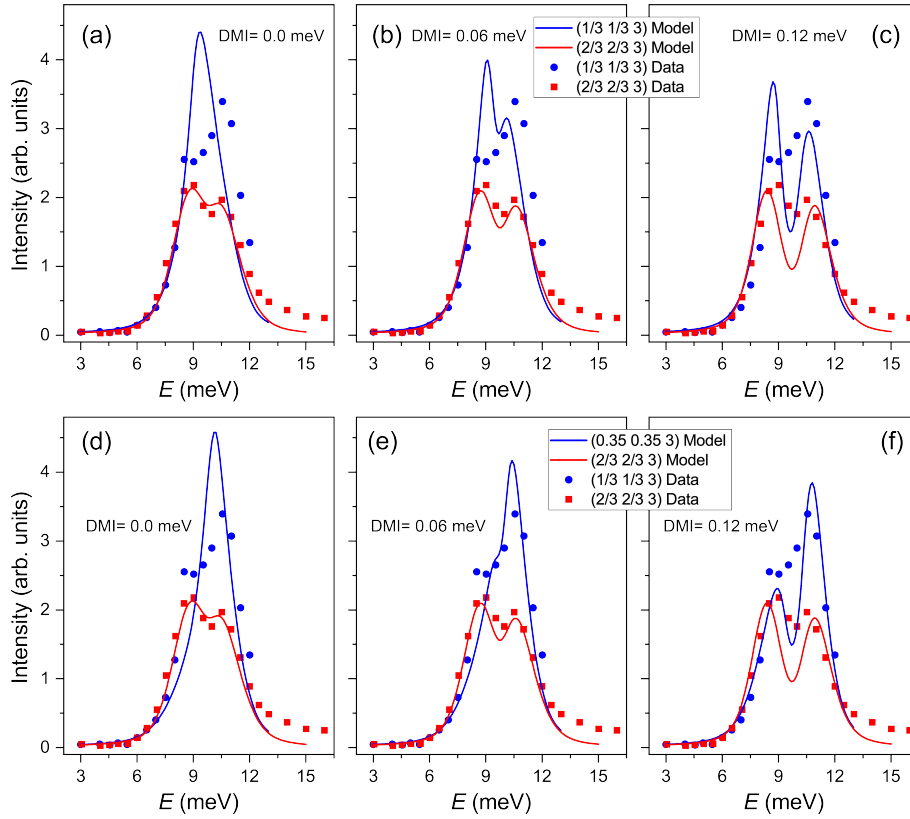


FIG. S6. Comparison of calculated spectrum with varying DMI size and experimental data from a *triple-axis* spectrometer experiment for  $\text{CrSiTe}_3$  [7]. The blue (red) filled circles are experimental constant momentum scan data at  $\text{K}_1$  ( $\frac{1}{3}, \frac{1}{3}, 3$ ) ( $\text{K}_2$  ( $\frac{2}{3}, \frac{2}{3}, 3$ )), digitized from Ref.[7]. (a-c) The blue and red solid lines are calculated spectrum at  $\text{K}_1$  ( $\frac{1}{3}, \frac{1}{3}, 3$ ) and  $\text{K}_2$  ( $\frac{2}{3}, \frac{2}{3}, 3$ ), respectively for the Heisenberg Hamiltonian parameters with DMI from 0 meV to 0.12 meV as described in the text, including instrumental resolution-convolution of the experimental conditions used in Ref.[7]. (d-h) The blue and red solid lines are calculated spectrum at  $\text{K}_1$  (0.35, 0.35, 3) and  $\text{K}_2$  ( $\frac{2}{3}, \frac{2}{3}, 3$ ).

## VI. REINTERPRETATION OF DMI SIZE IN $\text{CRSITE}_3$

In this section, we discuss the previously published triple-axis neutron spectroscopy results of  $\text{CrSiTe}_3$  [7]. As described in the main text, the spectrum at the K-point depends strongly on the shape of the resolution function. Figure S7 demonstrates how the resolution ellipses couple to magnon dispersions at the K-points and how it determines the focused and defocused regions. We assumed that the collected constant momentum scan at  $\text{K}_1$  in Ref. [7] was measured in the focused region, and compare the experimental data with spectrum simulated with varying DMI in accurate resolution-convolved spin-wave calculations for  $\text{CrSiTe}_3$ .

Figure S6 shows the simulated spin-wave spectra for  $\text{CrSiTe}_3$  [7], including the resolution calculation for the experiment using Reslib [5]. For the pin-wave calculation, we used Heisenberg spin Hamiltonian parameters ( $J_1 = -1.49$  meV,  $J_2 = -0.15$  meV,  $J_{c1} = -0.07$ ,  $J_{c2} = -0.06$ , and  $D^z = -0.01$  meV) from Ref. [7] with the second n.n. DMI = 0 meV, 0.06 meV, and 0.12 meV. Figure S6 (a-c) compare the resulting simulations with the experimental data at  $\text{K}_1$  ( $\frac{1}{3}, \frac{1}{3}, 3$ ) and  $\text{K}_2$  ( $\frac{2}{3}, \frac{2}{3}, 3$ ). For the zero DMI model, the simulated constant momentum scan at  $\text{K}_1$  (focused region) shows a single peak cor-

responding to a gapless Dirac magnon spectrum (solid blue line in Fig.S6(a)), but its line shape is narrower than data, the simulated intensity is shifted to lower energies, and it does not explain the peak splitting observed in the experimental data (blue filled circles). For non-zero DMI, the calculated spectrum opens a gap which generates two peaks, and the size of the gap increases as the strength of DMI increases. However, we note that the line shape of the simulated peaks for all the DMI values up to 0.12 meV do not match the experimental data: the intensity ratio between lower and upper magnon bands is reversed when compared to the experimental data. In practice, the measured wave vector can slightly deviate from exact K-point, ( $\frac{1}{3}, \frac{1}{3}, 3$ ), or the crystal can be slightly mis-aligned. To obtain better agreement with the data, we also simulate the spectrum at  $\mathbf{Q} = (0.35, 0.35, 3)$ . The simulated spectrum at this wave vector better reproduces not only the measured peak intensity distribution but also line shape observed for  $\text{K}_1^{\text{focus}}$ . Through a qualitative comparison with experimental data, we found that DMI = 0.06 meV provides a good description of the observed peak splitting and line shape [Fig. S6(e)]. On the other hand, in the  $\text{K}_2$  defocused region, the line shape is much less-sensitive to the DMI value and both 0 meV and 0.06 meV provide good agreement with the data. We note that 0.12 meV (the estimated best parameter in

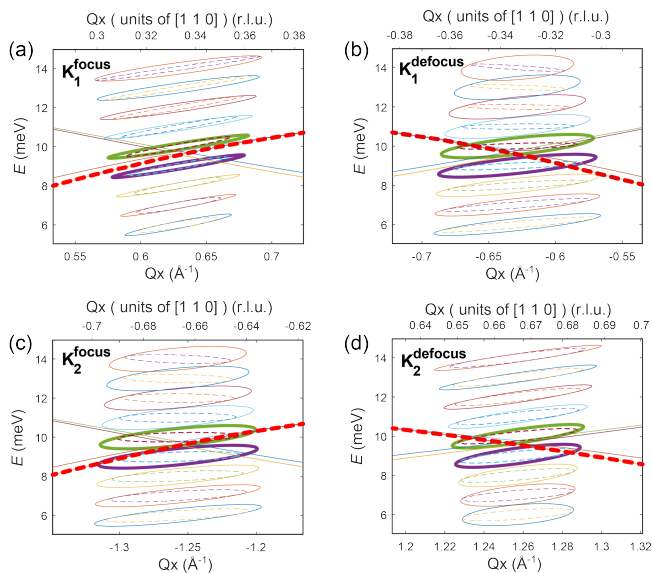


FIG. S7. Resolution ellipses and coupling to magnon dispersions for constant momentum scans at (a)  $K_1^{\text{focus}}$ , (b)  $K_2^{\text{defocus}}$ , (c)  $K_1^{\text{defocus}}$ , and (d)  $K_2^{\text{focus}}$  for the IN8 *triple-axis* spectrometer experiment for  $\text{CrSiTe}_3$  [7]. At each energy transfer plotted, the solid (dashed) ellipses correspond to the projection (section) of the resolution function onto the  $Q_x$ - $E$  plane. The solid lines are magnon dispersions of  $\text{CrSiTe}_3$ . The red thick dashed lines and thick ellipses indicate intense magnon modes and resolution functions coupled with the magnons at K-points. As a result of the coupling, the K-points are divided into ‘focus’ and ‘defocus’ regions according to whether the intense dispersion is parallel to and anti-parallel to the ellipse, respectively.

Ref.[7]) does not provide good agreement with the data.

- 
- [1] O. Arnold, J. Bilheux, J. Borreguero, A. Buts, S. Campbell, L. Chapon, M. Doucet, N. Draper, R. Ferraz Leal, M. Gigg, V. Lynch, A. Markvardsen, D. Mikkelsen, R. Mikkelsen, R. Miller, K. Palmen, P. Parker, G. Passos, T. Perring, P. Peterson, S. Ren, M. Reuter, A. Savici, J. Taylor, R. Taylor, R. Tolchenov, W. Zhou, and J. Zikovsky, Mantid—Data analysis and visualization package for neutron scattering and  $\mu\text{SR}$  experiments, Nuclear Instruments and Methods in Physics Research Section A: Accelerators, Spectrometers, Detectors and Associated Equipment **764**, 156 (2014).
- [2] R. Azuah, L. Kneller, Y. Qiu, P. Tregenna-Piggott, C. Brown, J. Copley, and R. Dimeo, Dave: A comprehensive software suite for the reduction, visualization, and analysis of low energy neutron spectroscopic data, J. Res. Natl. Inst. Stan. Technol. **114**, 341 (2009).
- [3] R. Ewings, A. Buts, M. Le, J. Van Duijn, I. Bustinduy, and T. Perring, Horace: software for the analysis of data from single crystal spectroscopy experiments at time-of-flight neutron instruments, Nuclear Instruments and Methods in Physics Research Section A: Accelerators, Spectrometers, Detectors and Associated Equipment **834**, 132 (2016).
- [4] S. Toth and B. Lake, Linear spin wave theory for single-q incommensurate magnetic structures, Journal of Physics: Condensed Matter **27**, 166002 (2015).
- [5] E. Farhi, Y. Debab, and P. Willendrup, iFit: A new data analysis framework. Applications for data reduction and optimization of neutron scattering instrument simulations with McStas, Journal of Neutron Research **17**, 5 (2014).
- [6] M. Popovici, On the resolution of slow-neutron spectrometers. IV. The triple-axis spectrometer resolution function, spatial effects included, Acta Crystallographica Section A **31**, 507 (1975).
- [7] F. Zhu, L. Zhang, X. Wang, F. J. dos Santos, J. Song, T. Mueller, K. Schmalzl, W. F. Schmidt, A. Ivanov, J. T. Park, J. Xu, J. Ma, S. Lounis, S. Blügel, Y. Mokrousov, Y. Su, and T. Brückel, Topological magnon insulators in two-dimensional van der Waals ferromagnets  $\text{CrSiTe}_3$  and  $\text{CrGeTe}_3$ : Toward intrinsic gap-tunability, Science Advances **7**, eabi7532 (2021).
- [8] P. R. Bevington and D. K. Robinson, Data reduction and error analysis, McGraw Hill, New York (2003).
- [9] L. Chen, J.-H. Chung, T. Chen, C. Duan, A. Schneidewind, I. Radelytskyi, D. J. Voneshen, R. A. Ewings, M. B. Stone, A. I. Kolesnikov, B. Winn, S. Chi, R. A. Mole, D. H. Yu, B. Gao, and P. Dai, Magnetic anisotropy in ferromagnetic  $\text{CrI}_3$ , Phys. Rev. B **101**, 134418 (2020).
- [10] E. J. Samuelsen, R. Silbergliitt, G. Shirane, and J. P. Remeika, Spin Waves in Ferromagnetic  $\text{CrBr}_3$  Studied by Inelastic Neutron Scattering, Phys. Rev. B **3**, 157 (1971).
- [11] D.-H. Kim, K. Kim, K.-T. Ko, J. Seo, J. S. Kim, T.-H. Jang, Y. Kim, J.-Y. Kim, S.-W. Cheong, and J.-H. Park, Giant Magnetic Anisotropy Induced by Ligand  $LS$  Coupling in Layered Cr Compounds, Phys. Rev. Lett. **122**, 207201 (2019).

- [12] L. Chen, J.-H. Chung, M. B. Stone, A. I. Kolesnikov, B. Winn, V. O. Garlea, D. L. Abernathy, B. Gao, M. Augustin, E. J. G. Santos, and P. Dai, Magnetic Field Effect on Topological Spin Excitations in  $\text{CrI}_3$ , *Phys. Rev. X* **11**, 031047 (2021).
- [13] S. A. Owerre, A first theoretical realization of honeycomb topological magnon insulator, *Journal of Physics: Condensed Matter* **28**, 386001 (2016).